SM Report 93-41

DTIC
ELECTE
MAY 3 1 1994
S F D

AD 279 791

FULL FIELD MEASUREMENTS OF THE DYNAMIC DEFORMATION FIELD AROUND A GROWING ADIABATIC SHEAR BAND AT THE TIP OF A DYNAMICALLY LOADED CRACK OR NOTCH

J.J. Mason
A.J. Rosakis
G. Ravichandran

Accesion For	
NTIS CRA&I	✓
DTIC TAB	
Unannounced	
Justification	
By	
Distribution /	
Availability Codes	
Dist	Avail and / or Special
A-1	

This document has been approved for public release and sale; its distribution is unlimited.

Graduate Aeronautical Laboratories
California Institute of Technology
Pasadena, CA 91125

Full Field Measurements of the Dynamic Deformation Field Around a Growing Adiabatic Shear Band at the Tip of a Dynamically Loaded Crack or Notch

James J. Mason,[1] Ares J. Rosakis and G. Ravichandran
California Institute of Technology,
Mail Code 105-50,
Pasadena, CA 91125

Abstract

The method of Coherent Gradient Sensing (CGS) is used to record the deformation field around an adiabatic shear band emanating from a pre-crack tip in C-300 steel loaded dynamically in mode-II. At early times after impact, the resulting fringe pattern surrounding the shear band seems to exhibit the deformation characteristics of a mode-II Dugdale plastic zone evolving under small scale yielding conditions, and, as a result, the experimental fringe patterns are fitted to the theoretical Dugdale crack deformation field by using a least squares fitting scheme. This results in values for the shear band length and the average shear stress acting on the shear band as functions of time. The shear band is observed to initiate when $K_{II}^{d}(t) = 140\ MPa\sqrt{m}$ and subsequently propagate with an average speed of 320 m/s. The average shear stress on the shear band decreases from 1.6 GPA at initiation to 1.3 GPa during the later stages of propagation.

---

[1] Currently with the Department of Aerospace and Mechanical Engineering, University of Notre Dame, Notre Dame, IN, 46556

1. Introduction

The formation of adiabatic shear bands has recently received renewed attention following the experimental measurements of the temperature rise in such bands by Duffy (1984). In the past ten years these measurements have helped motivate a considerable amount of modeling of adiabatic shear band growth which has recently appeared in the open literature. Without presenting an extensive review, it is helpful to recall some of the salient and common features of the many models that have been made available.

Commonly, the formation or growth of an adiabatic shear band is modeled as the competition between thermal softening and strain and/or strain-rate hardening of a material under shear loading. Usually an approximate model of thermal softening is added to the constitutive equation for a material, the temperature is treated as an additional unknown and the heat conduction equation is added to the field equations. Invariably, the heat conduction equation contains a term that links plastic deformation of the material to the production of heat (see Mason et al., 1992b), and a temperature rise in the material is predicted as a result of the deformation. The net effect of the assumptions of the model is the introduction of a mathematical mechanism by which instabilities in the deformation can be formed. When thermal softening is dominant over strain and/or strain-rate hardening, the material deforms, heats and becomes softer resulting in more deformation and the generation of more heat which further softens the material producing a "self-feeding" mechanism by which an instability is formed. The purpose of this work is to examine the deformation field around an adiabatic shear band as it forms and, hopefully, extract more information about the shear band formation process itself.

Kalthoff (1987) and Kalthoff and Winkler (1987) have observed the formation of adiabatic shear bands at the tip of dynamically loaded, stationary, pre-manufactured notches in plates made of high strength maraging steel. The pre-manufactured notches were loaded dynamically in nearly pure mode-II loading conditions by an asymmetric impact

in the area between the two pre-notches on the edge of the plate. See Figure 1(a). When sufficient impact velocity was used, an adiabatic shear band was formed directly ahead of the pre-notch as shown schematically in the figure. In the work described here, a similar configuration is used. This configuration involves the dynamic asymmetric loading of only *one* pre-notch and is schematically shown in Figure 1(b). The use of only one pre-notch provides a simple loading geometry by which one may observe the formation of adiabatic shear bands.

The method of Coherent Gradient Sensing (CGS) [Tippur et al. (1989a) and (1989b) and Rosakis (1993a)] is used here in reflection on pre-notched steel plates loaded dynamically in mode-II as described above. It is important to note that CGS has never before been used in a reflection arrangement to study deformations such as these. However, it has been used successfully in *transmission* for the study of mode-I dynamic crack growth [Tippur et al. (1989a) and (1989b)] and for the study of asymetric impact induced crack initiation in prenotched PMMA plates. [Mason et al., (1992a)].

It is proposed here that the shear band formation at a dynamically loaded mode-II pre-notch may be modeled by the Dugdale strip yield model. In such a model the shear band is assumed to be a one-dimensional line of yielded material evolving directly ahead of the stationary pre-notch or pre-crack with a uniform shear stress acting upon it. Implicit in this approach to modeling are a number of assumptions about the mechanisms of the nucleation and growth of adiabatic shear bands. For example, the following assumptions are made; the width of the shear band is assumed negligible, the shear band is assumed to grow straight ahead of the pre-notch or pre-crack, the shear stress is not allowed to vary over the length of the shear band, the effects of inertia are neglected in the interpretation of optical patterns, and the length of the shear band is determined by the far field $K_{II}^{d}(t)$ that is acting on the pre-notch (small scale yielding is implied and the magnitude of the shear stress on the yielded zone is chosen to nullify the highest order stress singularity at

the shear band tip).

The last of these assumptions is perhaps the most restrictive, however it is useful because it gives a relation between the stress intensity factor, the shear stress on the yield zone and the length of the yield zone. In addition it is also motivated by numerical investigations of dynamic shear band growth [Lee (1990)] where no singularity is found to exist at the growing shear band tip. For a pure $K_{II}^{d}(t)$ field with a Dugdale zone having a spatially uniform shear stress, $\tau_0(t)$, acting on it, the length of the yield zone, $R(t)$, is given by Rice (1968)

$$R(t) = \frac{\pi}{8}\left(\frac{K_{II}(t)}{\tau_0(t)}\right). \tag{1}$$

Although the assumptions and approximations of the model are somewhat limiting, the model is used here as a first attempt at analyzing the results, and it should be emphasized that the quantitative conclusions are reported as *first estimates* .

2. Experimental Procedure

2.1 The Method of CGS

A schematic of the CGS set-up is shown in Figure 3. A coherent, collimated laser beam, 50 mm in diameter, is reflected from a highly polished and initially flat surface of a prenotched opaque specimen. After the specimen is deformed, the non-uniform contraction at the vicinity of the pre-notch (or better the resulting shear band) causes the initially parallel bundle of light to deviate from parallelism after reflection. This is equivalent to acquiring an optical path difference due to the additional distance traveled by the initially planar wavefront in regions of the specimen where out of plane displacements occur. After reflecting from the deformed specimen, the beam impinges on the first of two identical diffraction gratings (40 lines/mm). The primary grating splits the beam into a direct beam and numerous diffraction orders. For the sake of brevity, only the first

diffraction orders (± 1) and the direct beam are considered. The second diffraction grating diffracts both the direct beam and the first diffraction orders into three beams each, giving a total of nine beams behind the second grating. Of these nine beams the (0,$\pm$1) and the ($\pm$1,0) orders are parallel—as can be seen in Figure 2.

An on-line spatial filter is used to isolate one of the two pairs of parallel beams. A lens is placed a distance equal to its focal length behind the secondary grating as in Figure 3. The Fourier Transform of the intensity distribution at the second grating is observed in the back-focal plane of the lens where an aperture is placed on either the +1 or -1 diffraction order spot. The aperture filters all but the two desired parallel beams from the wavefront. Another lens is placed at a distance equal to its focal length behind the aperture to invert the Fourier transformation.

It is assumed that the wave front before the first grating is approximately planar with some phase difference, $S(x_1, x_2)$. This phase difference is introduced because of the out of plane deformations on the specimen surface. Deviations of the propagation direction from the optical axis are neglected. Thus, the two gratings shift one beam with respect to the other by a distance

$$\epsilon = \Delta tan\theta \approx \Delta\theta \tag{2}$$

where Δ is the separation between the gratings, see Figure 3, and θ is the angle of diffraction (assumed small), given here by

$$\theta = sin^{-1}\frac{\lambda}{p} \approx \frac{\lambda}{p}\,. \tag{3}$$

λ is the wavelength of the illumination, and p is the pitch of gratings.

The two parallel, sheared wavefronts constructively interfere at a point if their difference in phase is an integer multiple of the wavelength, i.e., if

$$S(x_1 + \epsilon, x_2) - S(x_1, x_2) \;=\; m\lambda, \tag{4a}$$

where m is called "the fringe order." Dividing this equation by ϵ gives

$$\frac{S(x_1+\epsilon,x_2)-S(x_1,x_2)}{\epsilon} = \frac{m\lambda}{\epsilon}, \tag{4b}$$

which, for sufficiently small ϵ, may be approximated by

$$\frac{\partial(S(x_1,x_2))}{\partial x_\alpha} = \frac{mp}{\Delta}. \tag{5}$$

In equation (5), the approximations in equations (2) and (3) have been used, and the result has been generalized to include shearing in either the x_1 or x_2 direction, $\alpha = 1,2$.

Equations (4a) and (4b) are the standard equations for lateral shearing interferometry found in Murty (1978). Note that as ϵ goes to zero the approximation in equation (5) grows more exact, but at the same time the number of fringes and, therefore, the sensitivity of the system, is decreased. It is important that the grating separation, Δ, and, consequently, the value of ϵ, appropriately balances the competition between maximizing sensitivity and approximating the derivative.

For an opaque material reflecting the incident laser light, the phase difference, $S(x_1,x_2)$, in equation (5), is given by the difference in optical path length. This change is wholly attributed to changes in specimen thickness due to lateral contraction, and, thus, the optical path difference is given by [Tippur et al. (1989a) and (1989b) and Rosakis (1993a)]

$$\begin{aligned} S(x_1,x_2) &= 2h\int_0^{\frac{1}{2}} \epsilon_{33} d\left(\frac{x_3}{h}\right) \\ &= 2h\int_0^{\frac{1}{2}} \left\{(\sigma_{11}+\sigma_{22})\left[1-\frac{\sigma_{33}}{\nu(\sigma_{11}+\sigma_{22})}\right]\right\} d\left(\frac{x_3}{h}\right) \end{aligned} \tag{6}$$

where h is the thickness and the factor of 2 accounts for the light traveling the surface displacement twice, once on the way in and once on the way out. The integral represents the optical path difference due to changes in the plate thickness caused by the strain component, ϵ_{33}.

Assuming the material is isotropic and linearly elastic and using the plane stress assumption, $\sigma_{33}/\nu(\sigma_{11}+\sigma_{22}) \ll 1$, Eq (6) may be integrated giving the following result;

$$u_3 = -\frac{\nu h}{2E}(\hat{\sigma}_{11}+\hat{\sigma}_{22}) \tag{7}$$

where the term in brackets in Eq (6) has been neglected for plane stress conditions and $\hat{\sigma}_{11}$ and $\hat{\sigma}_{22}$ are plane stress thickness averages of stress components in the material while $\hat{\sigma}_{33} = 0$. Hence, inserting Eq (7) into Eq (6) gives

$$S(x_1, x_2) \approx 2u_3 = -\frac{\nu h}{E}(\hat{\sigma}_{11}+\hat{\sigma}_{22}) \,. \tag{8}$$

Finally, substituting (8) into (5) gives the result,

$$2\frac{\partial u_3}{\partial x_\alpha} = -\frac{\nu h}{E}\frac{\partial(\hat{\sigma}_{11}+\hat{\sigma}_{22})}{\partial x_\alpha} \approx \frac{mp}{\Delta}. \tag{9}$$

All interference images produced by the CGS apparatus in this work are interpreted using equation (9). Notice that a rigid body rotation does not effect the results since the derivative of u_3 of such a motion results in a constant that has no effect upon fringe pattern formation. The method of using an incident beam at a small angle to the undeformed-surface normal is made possible by this result. Angling the incident illumination is identical to a rigid body rotation. This fact precludes the need for a beam splitter in the set-up of CGS for use in reflection on opaque materials. In the experiments reported here the specimens were illuminated at a small angle to the undeformed-surface normal.

For the case of a semi-infinite Mode-II Dugdale crack with a yield zone of length $R(t)$ the solution for the elastic stresses around the yield zone may be found [Rice (1968)],

$$\hat{\sigma}_{11}(t) + \hat{\sigma}_{22}(t) = \frac{4\tau_0(t)}{\pi}\mathrm{Im}\left[\tan^{-1}\left(\sqrt{\frac{R(t)}{z-R(t)}}\right)\right] \tag{10}$$

where $\tau_0(t)$ is the shear stress on the yield zone and $z = x_1 + ix_2$ is a complex number. Taking the derivative of this function gives

$$\begin{aligned} \frac{\partial\left\{\hat{\sigma}_{11}(t)+\hat{\sigma}_{22}(t)\right\}}{\partial x_1} &= -\frac{2\tau_0(t)}{\pi}\mathrm{Im}\left[\frac{1}{z}\sqrt{\frac{R(t)}{z-R(t)}}\right], \\ \frac{\partial\left\{\hat{\sigma}_{11}(t)+\hat{\sigma}_{22}(t)\right\}}{\partial x_2} &= -\frac{2\tau_0(t)}{\pi}\mathrm{Re}\left[\frac{1}{z}\sqrt{\frac{R(t)}{z-R(t)}}\right]. \end{aligned} \tag{11}$$

Inserting this result in the governing equation for the CGS apparatus, Eq (9), results in an equation for the formation of fringes around a semi-infinite Mode-II Dugdale crack. This equation has been solved here numerically for partial differentiation in both directions, x_1 or x_2, and the results may be seen in Figure 4. For very large distances (when compared to the Dugdale zone size) away from the pre-crack tip the fringe pattern resembles the pattern for a pure mode-II K dominant field. (See the fringe patterns in Mason et al., 1992a.) Also, when partial differentiation with respect to x_1 is performed the fringe pattern gives a clear indication of the location of both the original pre-crack tip and the tip of the Dugdale zone. For this reason all experiments reported here are performed with differentiation parallel to the pre-crack tip, i.e., differentiation with respect to x_1. And quick estimates of the Dugdale zone size are made by measuring the distance between the point where the rear lobe converges to the x_1 axis and the point where the front lobes converge to the x_1 axis.

2.2 *Apparatus*

The exact specimen geometry is shown in Figure 5. Specimens are made of C-300 maraging steel. Impact of the specimens is achieved using an air gun and a 75 mm long, 50 mm diameter projectile made of C-350 maraging steel. Two types of test were performed; first, round tip pre-notches $\approx .5mm$ thick machined by wire EDM as per the figure were impact loaded, and, second, pre-cracks approximately 10 mm in length grown at the tip

of a 50 mm long, .5 mm thick pre-notch by loading the specimen in dynamic shear were impact loaded.

Set up of the CGS apparatus follows Figure 3. A high-speed framing camera manufactured by Cordin Co. (Salt Lake City, UT) is used as the imaging system. The CGS interferograms are generated using an Argon-Ion laser synchronized with the high-speed camera and pulsed for 50 ns at 1.4 μs intervals as the light source. The total length of the record of the event is $\approx$ 110 μs resulting in approximately 80 CGS interferograms per test.

The fringe patterns are digitized by hand. A ray of constant angle ϕ from the x_1 axis is followed; points at the center of fringes are digitized along the way. The effective crack tip was chosen by estimating the point where the rear lobe converged to the x_1 axis. See Figure 4(a). Most of the uncertainty in digitization arises from locating the effective crack tip and choosing the center of the fringe.

2.3 *Data Reduction*

Deviation of experimental results from the fringe patterns predicted by a mode-II Dugdale crack field are expected for many reasons. These include the existence of a zone around the pre-notch tip where plane stress assumptions break down (the 3-D zone) [Rosakis and Ravi-Chandar (1986) and Krishnaswamy et al. (1988)], the interference of propagating waves from the loading with the crack tip field and violation of the assumptions used in the derivation of the Mode-II Dugdale model. Consequently, the results are analyzed by *fitting* the Dugdale crack solution to the digitized fringes of the experiment by a least squares fitting scheme. Digitization is carried out only on the points above the pre-crack line (impact occurs on the side of the specimen *below* the pre-crack line) in order to avoid confusion caused by the interaction between the Dugdale zone pattern and the pattern generated by the propagating waves. The fit is produced by minimizing the

error function

$$\chi(\tau_0, R) = \sum_{i=1}^{N} (m_i - f(r_i, \theta_i))^2 , \tag{12}$$

where

$$f(r_i, \theta_i) = -\frac{\Delta}{p}\frac{\nu h}{E}\frac{\partial(\hat{\sigma}_{11} + \hat{\sigma}_{22})}{\partial x_\alpha} \tag{12a}$$

and

$$\begin{aligned} r_i &= \sqrt{x_1^2 + x_2^2} \\ \theta_i &= \tan^{-1}\left(\frac{x_2}{x_1}\right) \end{aligned} . \tag{12b}$$

The expression for the partial derivative in Eq (12) is given by Eq (11), and N is the total number of points. The minimization of equation (12) was performed numerically. First, the dynamic stress intensity factor was taken from the solution of Lee and Freund (1990). When the solution of Lee and Freund (1990) is no longer applicable, at longer times, a fit of the results in Mason et al. (1992a) for long times is used. This is justified by the agreement between the model and the experimentally measured $K_{II}^{d}(t)$ for PMMA loaded under the same conditions as demonstrated in Mason et al., (1992a). Then the function χ was minimized numerically with respect to the shear stress $\tau_0(t)$ while holding the stress intensity factor constant.

3. Results and Discussion

As a first investigation of the shear band formation, lines were etched on the steel, and it was impacted at 40 m/s. The resulting deformation can be seen in Figure 6. The shear band zone width is small, 200-300 μm, and the average shear strain in the band is roughly 100%. Note that the deformation is mostly elastic outside the shear band and that the etched lines above and below the shear band are still aligned as they were before the deformation. This fact indicates that during the shear band formation the lower, impacted plane of material is compressed elastically moving the lower half of the etched lines to the right while the upper plane of material remains approximately stationary with the shear

band absorbing the resultant mismatch deformation. After a crack forms along the shear band elastic unloading occurs allowing the lines to realign. This observation justifies the use of an elastic constitutive equation in the Dugdale crack model to predict the material deformation around the forming adiabatic shear band in future experiments.

Primary test were performed on pre-notched specimens. In spite of some ofthe shortcomings of the test, the results have some merit because the initiation and propagation of a shear band was seen in the photos and a change of failure propagation mode occurs at later times. A photograph of the specimen after the experiment is shown in Figure 7. The initial failure growth directly ahead of the pre-notch tip is a shear band dominated failure growth. No shear lips are observed and the failure surface is relatively smooth and shiny resembling that reported by Kalthoff (1987) and Kalthoff and Winkler (1987) for shear failure. This growth is observed in the recorded fringe patterns (not shown) and, in agreement with the report of Kalthoff (1987) and Kalthoff and Winkler (1987), the growth proceeds at a small negative angle, $\approx 5°$, to the x_1 axis. The shear-band growth is found to arrest at approximately 40 μs after impact of the specimen. This time corresponds roughly to the time required for an unloading wave from the rear of the projectile to reach the pre-notch or shear band tip. After the shear growth arrested, a different mode of failure is initiated at an large positive angle to the shear growth as can be seen in Figure 7. This growth is mode-I dominated as evident from the rough fracture surfaces and the shear lips visible in Figure 7(b), Initiation and growth of this latter crack occurs long after the recorded loading, and, unfortunately, the exact details of this very interesting failure mode transition, observed for the first time, are not yet known.

In Figure 8 a record of fringes may be seen for a dynamically loaded stationary *pre-crack*. Time $t = 0$ corresponds to the time of impact of the plate edge. Waves generated at the time of impact take approximately 12 μs to reach the pre-crack and begin loading. The deformation has a resemblance to the theoretical fringe pattern shown in Figure 4(a).

The "effective" crack tip and zone tip can be located by the fringe pattern in the upper half plane quite easily. However, the waves in the lower half plane considerably complicate the fringe pattern there at various times during the recorded deformation. Consequently, in order to simplify the digitization procedure, only the fringes on the upper half plane were digitized. It is felt that the upper fringes closely resemble the small scale yielding, Dugdale zone pattern throughout the recorded deformation because extensive interaction of the upper fringes with the incoming stress wave is not observed. Note, however, that the fringe pattern on the upper half-plane becomes less and less similar to the Dugdale pattern as time goes on. At 47 μs deviations between the measured fringe pattern and the theoretical pattern become too large to warrant further fitting of the theoretical Dugdale deformation field to the experimentally measured deformation field. Furthermore, the aperture spot (shadow area) forming around the shear zone continues to grow making it more and more difficult to record the fringe pattern.

In Figure 8 there is an aperture spot around the Dugdale zone and crack tip at longer times. It can be seen in Figure 8, after some analysis, that the pre-crack faces are coming into contact. The pre-crack is curved slightly downward, and the curved faced are being forced together by compressive loads acting in the x_1 direction. Consequently, the effective crack tip at early times is where the two faces initially come into contact and not at the actual initial pre-crack tip.

Because of the existence of the contact zone in this experiment, the shear band length, $R_{sb}(t)$ is defined here as the length of the fit Dugdale zone size, $R(t)$, less the contact zone length, $R_{cz}(t)$, which can be measured directly from the photographs. Hence,

$$R_{sb}(t) = R(t) - R_{cz}(t)$$

where the contact zone length is found by measuring the distance between the zero point indicated by the fringe pattern and the initial pre-crack tip and $R(t)$ is produced by the fit indicated in Eq (12). The pre-crack faces are in contact at t=26 μs ($c_d t/l = 2.3$), and the

Dugdale fringe pattern indicates that the shear zone extends to the initial pre-crack tip at that time. Consequently, at time t=26 μs, $R_{sb}(t) = 0$, and from then on a shear band is observed.

Fits were performed for photos taken at the times 17–47 μs after impact. Photographs taken at earlier times either showed no loading or did not show enough loading to warrant a useful fit. An example of one of the fits (performed at 31.5 μs) can be found in Figure 10. Acceptable agreement between the theoretical Dugdale field and the experimentally measured field is seen.

The results of the fit for the shear stress on the shear band, $\tau_0(t)$, and for the shear band length, $R_{sb}(t)$ are plotted in Figure 11. The shear band length increases with time, and a linear fit of the growth provides an estimate of the shear band growth velocity of 320 m/s. The initiation occurs at approximately 26 μs, $c_d t/l = 2.3$, well within the domain of the Lee and Freund (1990) solution. At this time the stress intensity is roughly 140 $MPa\sqrt{m}$. The shear stress increases initially with time from 0.6 GPa to 1.6 GPa before the shear band initiation. It is assumed that this effect is due to increasing load on the pre-crack faces that are already in contact. After the shear band is initiated, the shear stress decreases from 1.6 GPa to 1.3 GPa. This type of behavior is expected since thermal softening is the acting mechanism by which the shear band forms. As the shear band grows it is expected that the shear stress decreases due to thermal softening. Recent experiments conducted in the same geometry at Caltech indicate temperatures of up to 600°C above ambient at the tip of the propagating shearband. [Rosakis (1993b)] The value of the shear band length obtained from the fit described by equation (12) is compared to the estimated shear band length. This length is estimated from the photographs by comparing the recorded CGS fringe pattern to the predicted fringe pattern in Figure 4 as described in Section 2.1. Acceptable agreement is seen.

For comparison, the constitutive behavior of this material was measured and is shown

in Figure 12 for various strain rates. The curves were measured in uniaxial compression, but, for ease of comparison, the equivalent shear stress is plotted using the Von Mises criterion. In high strain rate tests, the formation of shear bands in the specimen is observed. The material hardens with strain initially, but at higher strains thermal softening becomes dominant and the measured stress decreases with strain. This is typical observed behavior for the formation of instabilities in a uniaxial test. Examination of the specimens after testing shows unmistakable evidence of shear band failure. Plotted with the Kolsky bar data is an estimate of the stress-strain behavior of the material within the shear band observed here. An estimate of the constitutive behavior of the material within the shear band may be obtained by using the reported stress values in Figure 11 and by estimating the corresponding average strains on the shear band. We assume that the relative shear displacements of the upper and lower shear band faces decrease linearly from th pre-crack tip to zero at the tip of the band (the end of the Dugdale zone). If the shear band also has a fised thickness, t_{sb}, then the average strain is given by

$$\epsilon = \frac{K_{II}^2}{2E\tau_0 t_{sb}}$$

This combined with the known values of the shear stress in Figure 11 gives a stress-strain relationship for the shear band materials which is displayed in Figure 12 along with the shear response curves obtained means of Kolsky bar experiments. Good agreement is found between the measured local stress-strain behavior of the shear band and the results of the Kolsky bar tests.

4. Conclusions

The formation of a shear band at the tip of a pre-crack loaded dynamically in mode-II has been recorded using high-speed photography and the method of CGS to examine the stress field around the pre-crack tip. It is seen that the recorded fringe patterns around the pre-crack correspond well with the theoretical pattern for a mode-II small scale yielding

Dugdale plastic zone model. Consequently, a fit of the digitized experimental fringe field is made to the Dugdale zone solution with the shear stress on the shear band as a parameter varying with time. The remote stress intensity factor is assumed to follow the model of Lee and Freund (1990). The results of the fits are used to extract the time evolution of the shear stress on the shear band and the length of the shear band with the following results:

It is seen that the shear band initiates within the regime of the Lee and Freund (1990) solution for this problem. However, it does not initiate at the first loading of the pre-notch tip. There is a time delay of approximately 11 μs, after the arrival of the compressive wave at the crack tip, before shear band growth is observed. The shear band initiates when $K_{II}^{d} = 140 MPa\sqrt{m}$.

The shear band propagates into the material with a speed of roughly 320 m/s while at the same time the shear stress on the shear band decreases from 1.6 GPa at initiation to 1.3 Gpa.

Acknowledgements

The on-going support of the Army Research Office under grant # DAAH04-93-G0037 and the support of the Office of Naval Research under grant #N00014-90-J-1340 are greatly appreciated.

References

1. J.Duffy (1984), Temperature measurements during the formation of shear bands in a structural steel, G.J. Dvorak and R.T. Shields, eds., *Mechanics of Material Behavior,* Elsevier Science Pub. B.V., Amsterdam, 75

2. F. Erdogan and G.C. Sih (1963), On the crack extension in plates under plane loading and transverse shear, *J. Basic Engineering,* **85**, 519

3. P. Hariharan, W. H. Steel and J.C. Wyant (1974), Double grating interferometer with variable lateral shear, *Optics Communications,* **11**, no. 3, 317

4. P. Hariharan and Z. S. Hegedus (1975), Double grating interferometers II. Application to collimated beams, *Optics Communications* **14**, no 1, 148

5. J.F. Kalthoff (1987), Shadow optical analysis of dynamic shear fracture, in: *SPIE Vol. 814 Photomechanics and Speckle Metrology,* 531

6. J.F. Kalthoff and S. Winkler (1987), Failure mode transition at high rates of shear loading, in: C.Y. Chiem, H.-D. Kunze and L.W. Meyer, eds., *Impact Loading and Dynamic Behavior of Materials,* Verlag, Vol. 1, 185

7. S. Krishnaswamy, A.J. Rosakis and G. Ravichandran (1988), On the extent of dominance of asymptotic elastodynamic crack-tip fields 2. Numerical investigation of 3-dimensional and transient effects, Caltech Report SM88-21, (*J. Appl. Mech.,* **58**, 95)

8. Y.J. Lee (1990), Problems associated with dynamic fracture under high strain rate loading, Ph.D. Thesis, Division of Engineering, Brown University, Providence, RI

9. Y.J. Lee and L.B. Freund (1990), Fracture initiation due to asymmetric impact loading of an edge cracked plate, *J. Applied Mechanics,* **57**, 104

10. J.J. Mason, J. Lambros and A.J. Rosakis (1992), The use of a coherent gradient sensor in dynamic mixed-mode fracture mechanics experiments, *J. Mech. Phys. Sol.,* **40**, No. 3, 641

11. J.J. Mason, A.J. Rosakis and G. Ravichandran (1992), On the strain and strain-rate dependence of the fraction of plastic work converted to heat: An experimental study using high speed infrared detectors and the Kolsky bar, *Solid Mechanics Report 92-33,* Graduate Aeronautical Laboratories, California Institute of Technology, Pasadena, CA 91125

12. M.V.R.K. Murty (1978), Lateral shearing interferometers, in: D. Malacara, ed., *Optical Shop Testing,* J. Wiley & Sons, Ch. 4.

13. J. R. Rice (1968), *Fracture,* Volume II, Academic Press, New York, Ch. 3, 264

14. A.J. Rosakis (1993a), Two optical techniques sensitive to gradients of optical path difference: The method of caustics and the coherent gradient sensor (CGS), in *Experimental Techniques in Fractures III,* J.S. Epstein, Ed., Society for Experimental Mechanics, Inc., Bethel, CT, Ch. 10

15. A.J. Rosakis (1993b), *Private Communication*

16. A.J. Rosakis and K. Ravi-Chandar (1986), On crack-tip stress state: an experimental evaluation of three-dimensional effects, *Int. J. Solids & Structures,* **22**, 121

17. H.V. Tippur, S. Krishnaswamy and A.J. Rosakis (1989a), A coherent gradient sensor for crack tip deformation measurements: analysis and experimental results, Caltech SM-Report 89-1, (*Int. J. Fracture,* **48**, 193)

List of Figures

Figure 1 (a) The loading geometry observed by Kalthoff (1987) and Kalthoff and Winkler (1987) to generate shear bands in C-300 steel at a pre-notch or pre-crack tip. (b) The modified pre-notched geometry used in the present investigation.

Figure 2 Schematic describing the working principle of CGS.

Figure 3 Schematic of the experimental set up for transmission CGS.

Figure 4 (a) Numerical predictions of CGS fringes (constant $\frac{\partial(\hat{\sigma}_{11}+\hat{\sigma}_{22})}{\partial x_1}$ values) constructed on the basis of a pure K_{II}^{d} field with a Dugdale shear zone of length R ahead of the pre-crack tip. (b) Predictions of CGS fringes for constant $\frac{\partial(\hat{\sigma}_{11}+\hat{\sigma}_{22})}{\partial x_2}$ values and the same assumptions as (a).

Figure 5 Specimen geometry, loading configuration and material constants.

Figure 6 Example of a shear band formed by asymmetric loading of a pre-notch. The lines were etched before loading. Shear localization is observed.

Figure 7 Photograph of the crack path taken after dynamic loading of a pre-notch. The crack propagates forward parallel to the pre-notch in a shear dominated mechanism then arrests. At later times the crack propagates at an angle to the pre-notch in a locally symmetric (mode-I) mode of failure.

Figure 8 Sequence of CGS interferograms corresponding to the initial stages of the dynamic asymmetric loading of a pre-cracked specimen impacted at 38 m/s.

Figure 9 The actual initial pre-crack tip, as indicated, and the "effective" initial crack tip can be seen in this photograph taken at t=31.5 μs.

Figure 10 A check of the fitting procedure for t=31.5 μsData points should fall alternately on light and dark fringes in the figure. It can be seen that the fit is reasonably good for the forward fringe with less agreement found for the rear fringe.

Figure 11 A plot of $\tau_0(t)$ and $R(t)$ as found from the fitting procedure in equation (12). The shear band length is compared to the length as estimated by comparing the fringe patterns in Figure 8 to the theoretical fringe pattern in Figure 4.

Figure 12 The constitutive behavior of C-300 at various strain rates as measured in compression. High strain rate data was measured using a Kolsky bar apparatus as shown in Mason et al. (1992b)

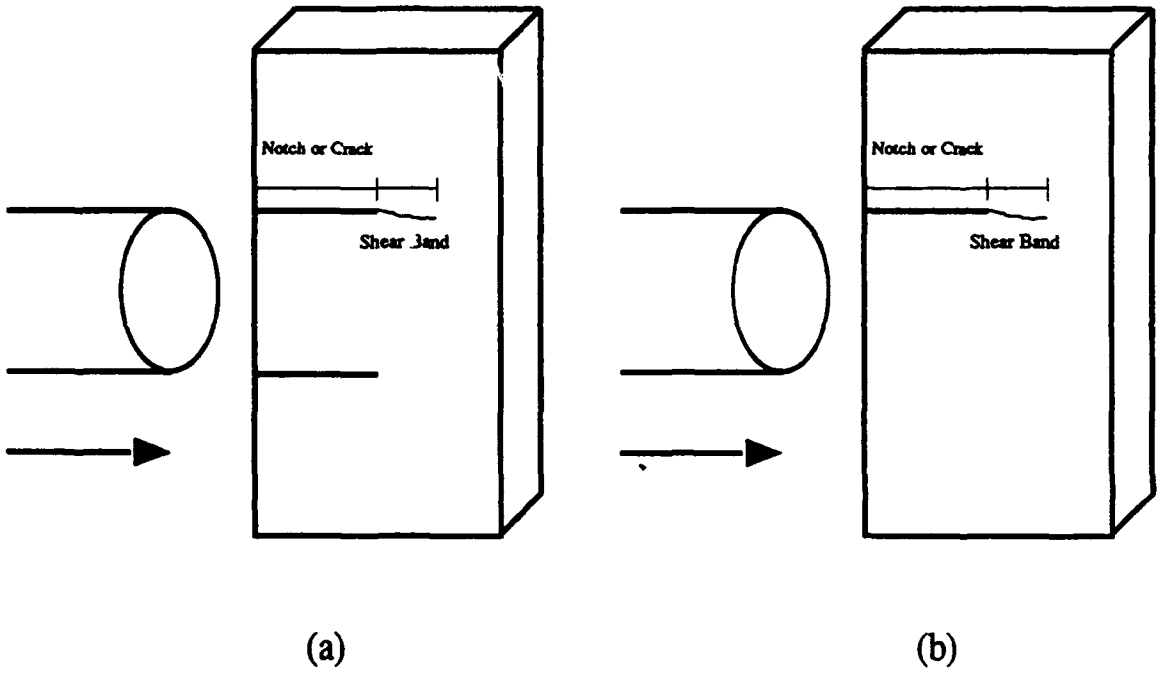

FIGURE 1 (a) The loading geometry observed by Kalthoff (1987) and Kalthoff and Winkler (1987) to generate shear bands in C-300 steel at a pre-notch or pre-crack tip. (b) The modified pre-notched geometry used in the present investigation.

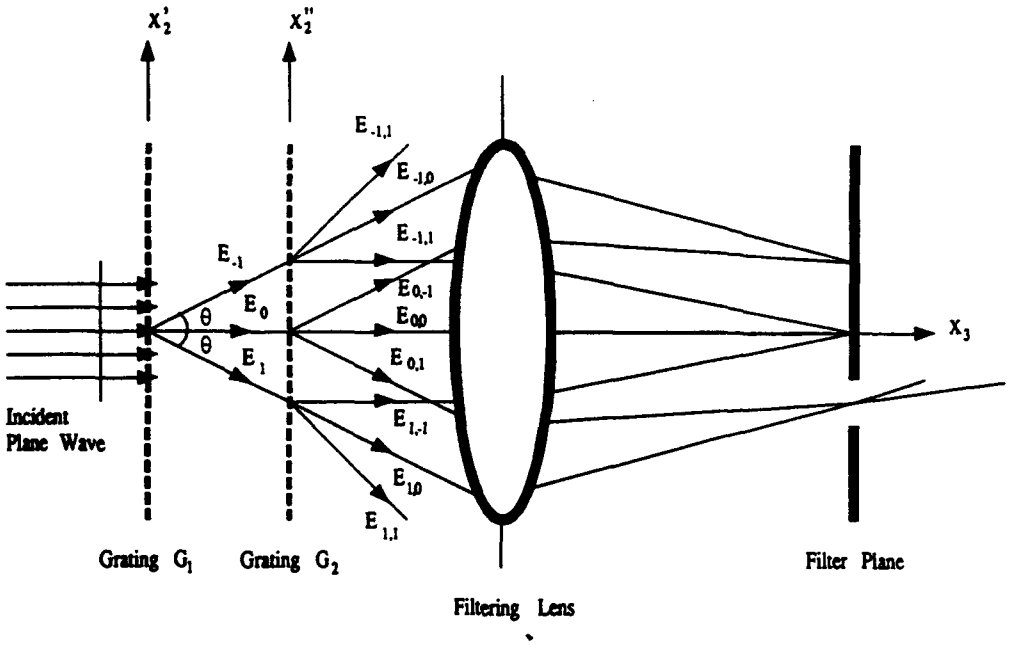

FIGURE 2 Schematic describing the working principle of CGS.

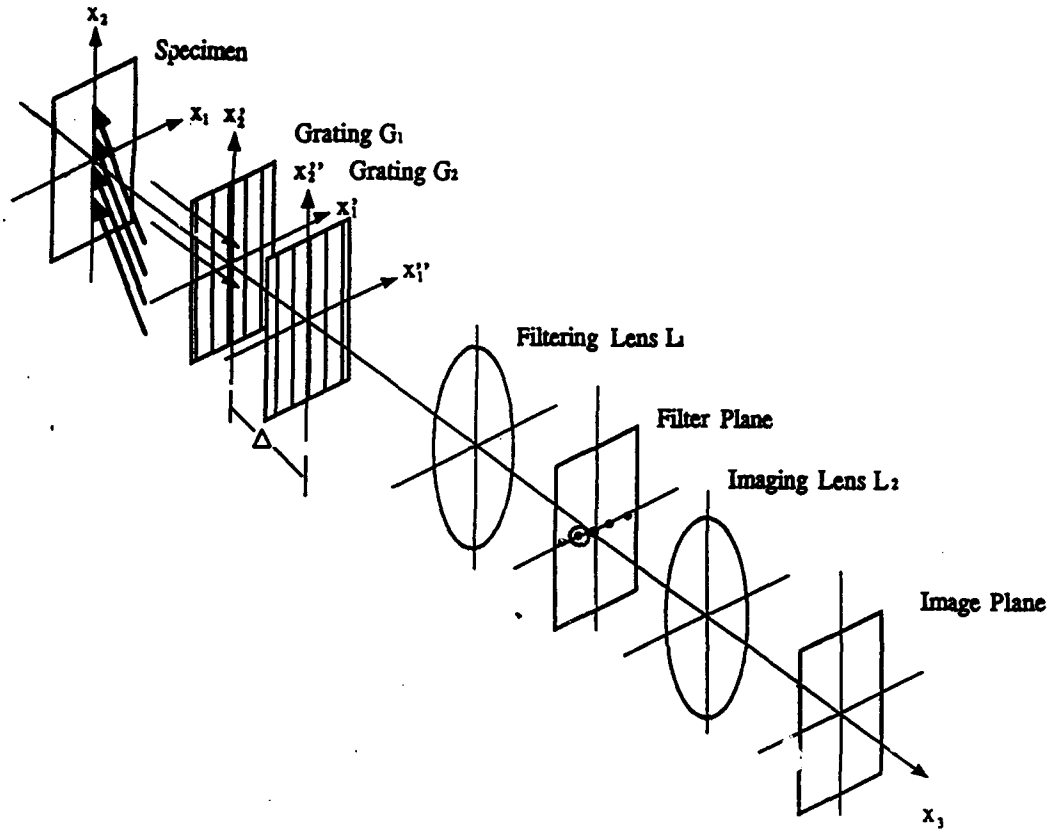

FIGURE 3 Schematic of the experimental set up for reflection CGS.

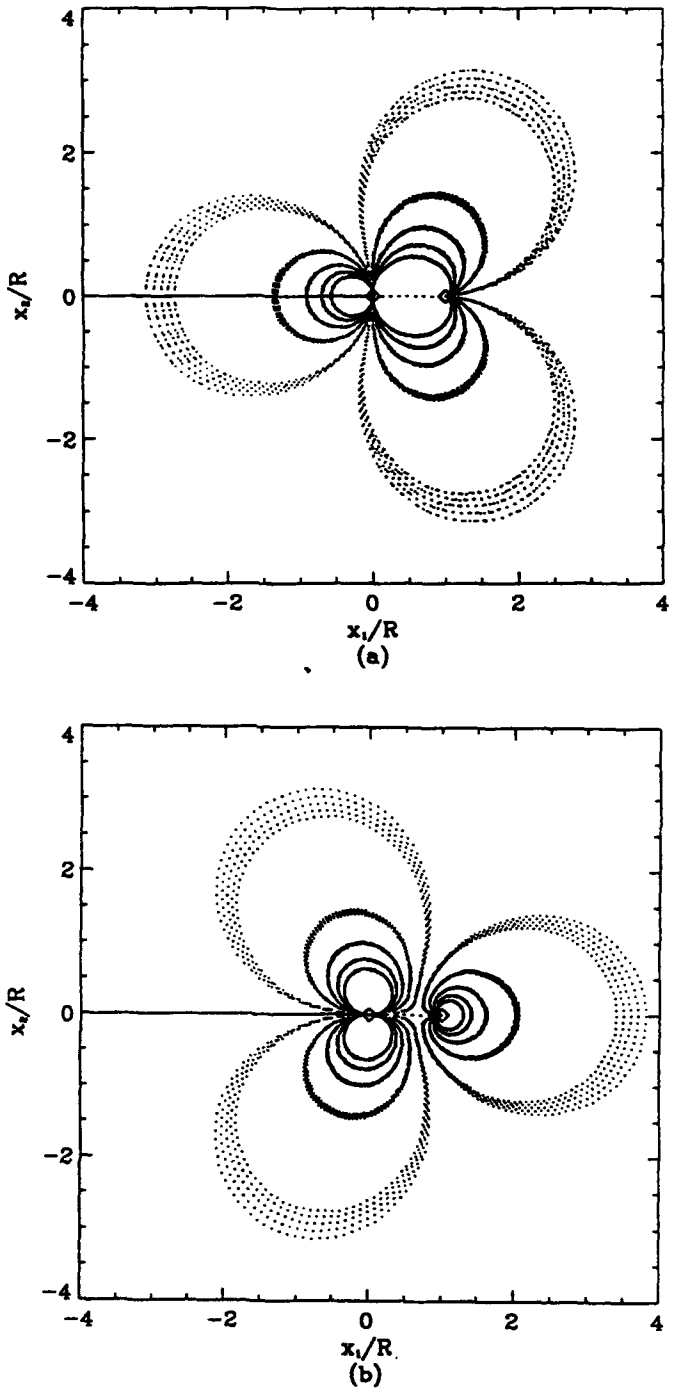

FIGURE 4 (a) Numerical predictions of CGS fringes (constant $\frac{\partial(\hat{\sigma}_{11}+\hat{\sigma}_{22})}{\partial x_1}$ values) constructed on the basis of a pure K_{II}^{d} field with a Dugdale shear zone of length R ahead of the pre-crack tip. (b) Predictions of CGS fringes for constant $\frac{\partial(\hat{\sigma}_{11}+\hat{\sigma}_{22})}{\partial x_2}$ values and the same assumptions as (a).

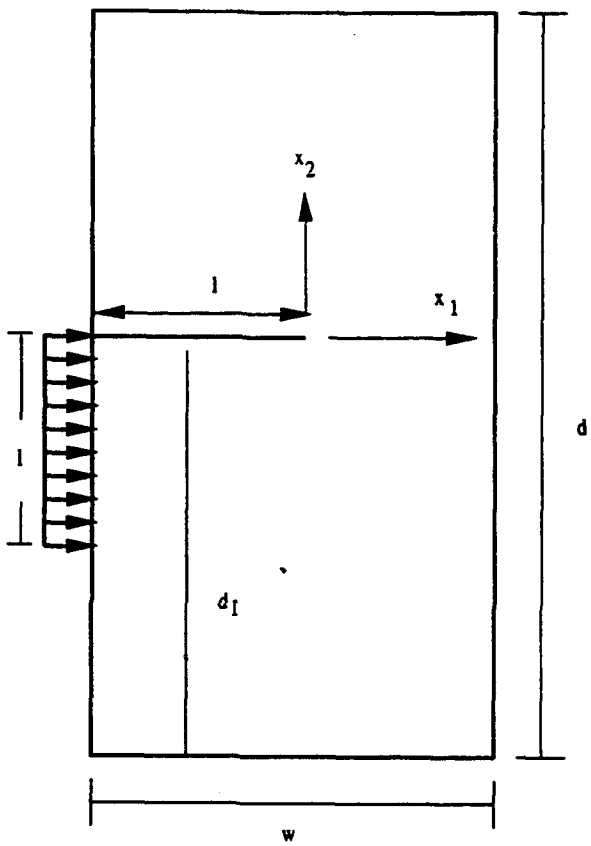

Dimensions of specimen:
l=50 mm
w=100 mm
d=200 mm
d_I=113 mm
thickness=6 mm

Mechanical Properties of specimen:
E=200 GPa
v=.3
c_d^{pl-o}=5430 m/s

FIGURE 5 Specimen geometry, loading configuration and material constants.

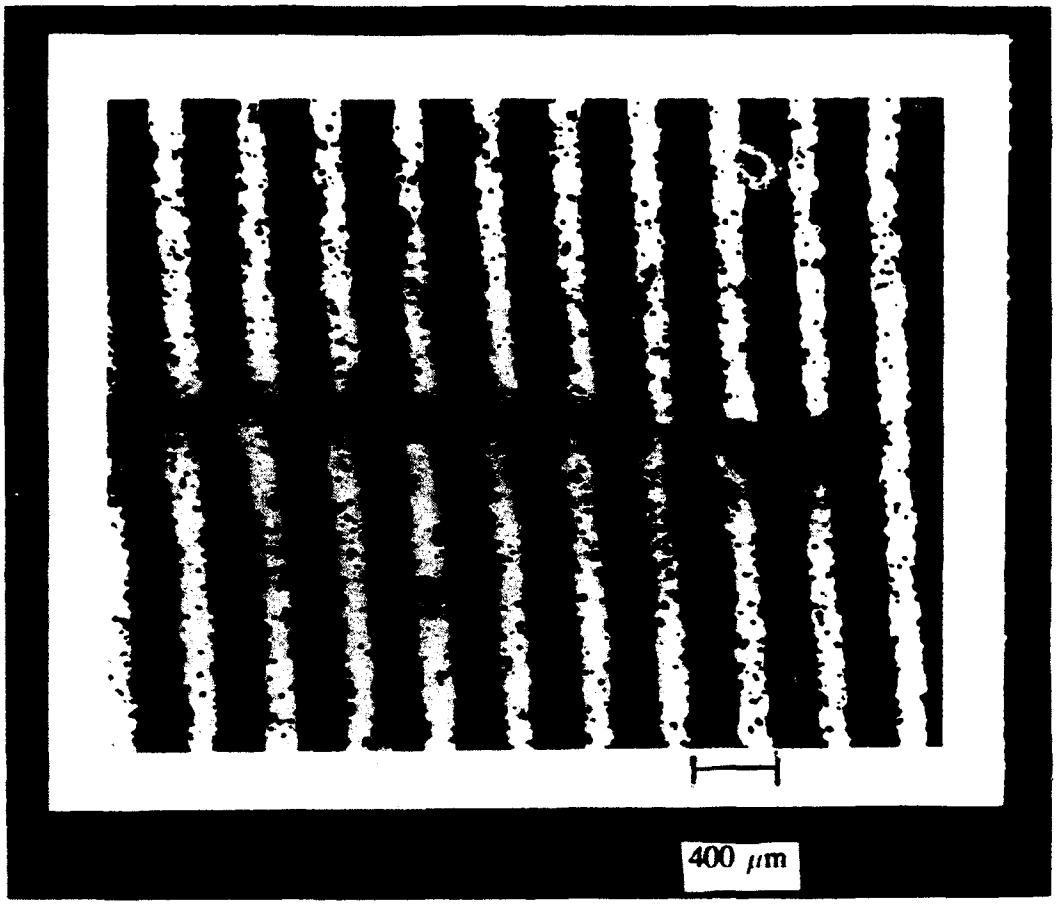

FIGURE 6 Example of a shear band formed by asymmetric loading of a pre-notch. The lines were etched before loading. Shear localization is observed.

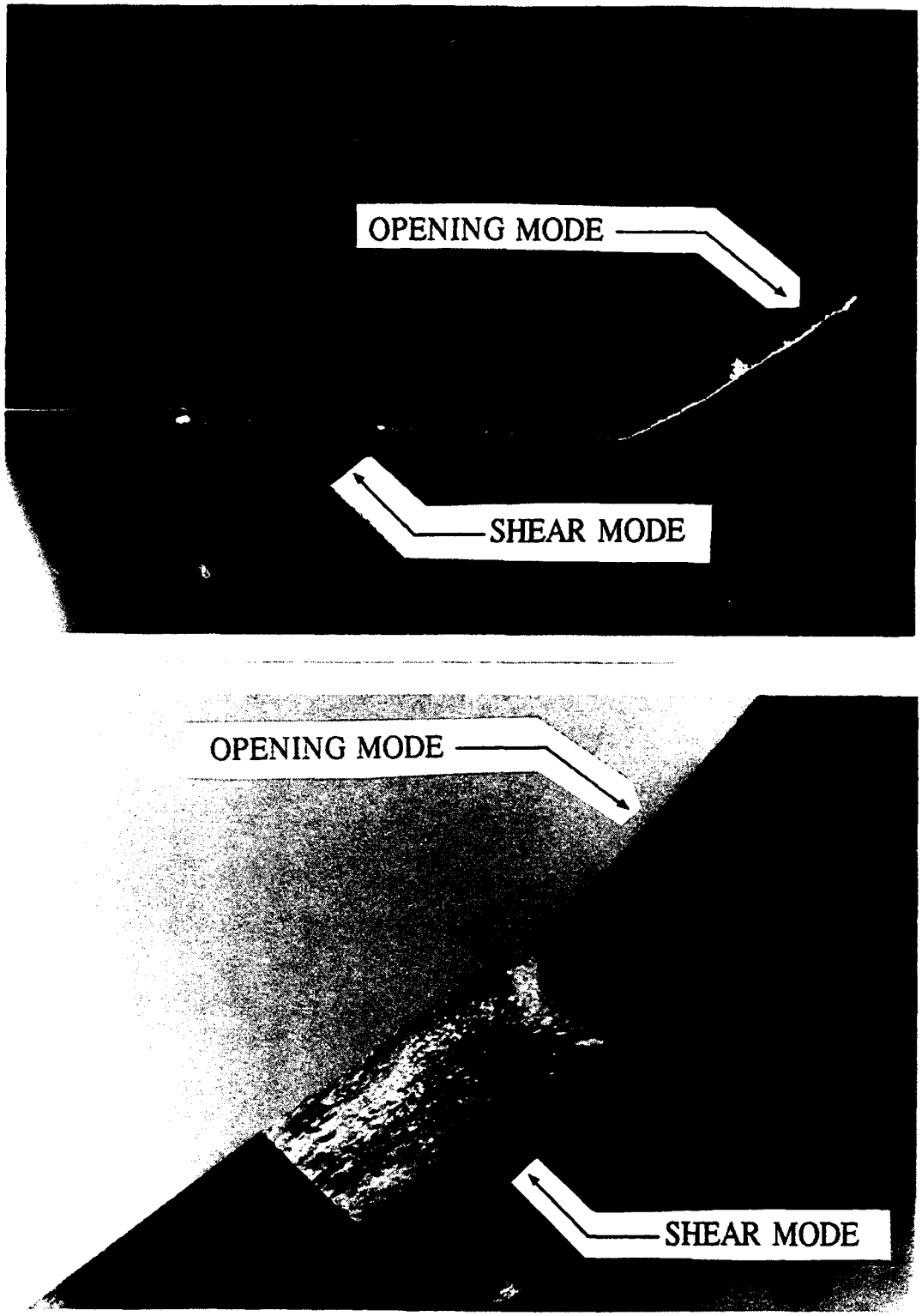

FIGURE 7 Photograph of the crack path taken after dynamic loading. The crack propagates forward parallel to the pre-notch in a shear dominated mechanism then arrests. At later times the crack propagates at an angle to the pre-notch in a locally symmetric (mode-I) mode of failure.

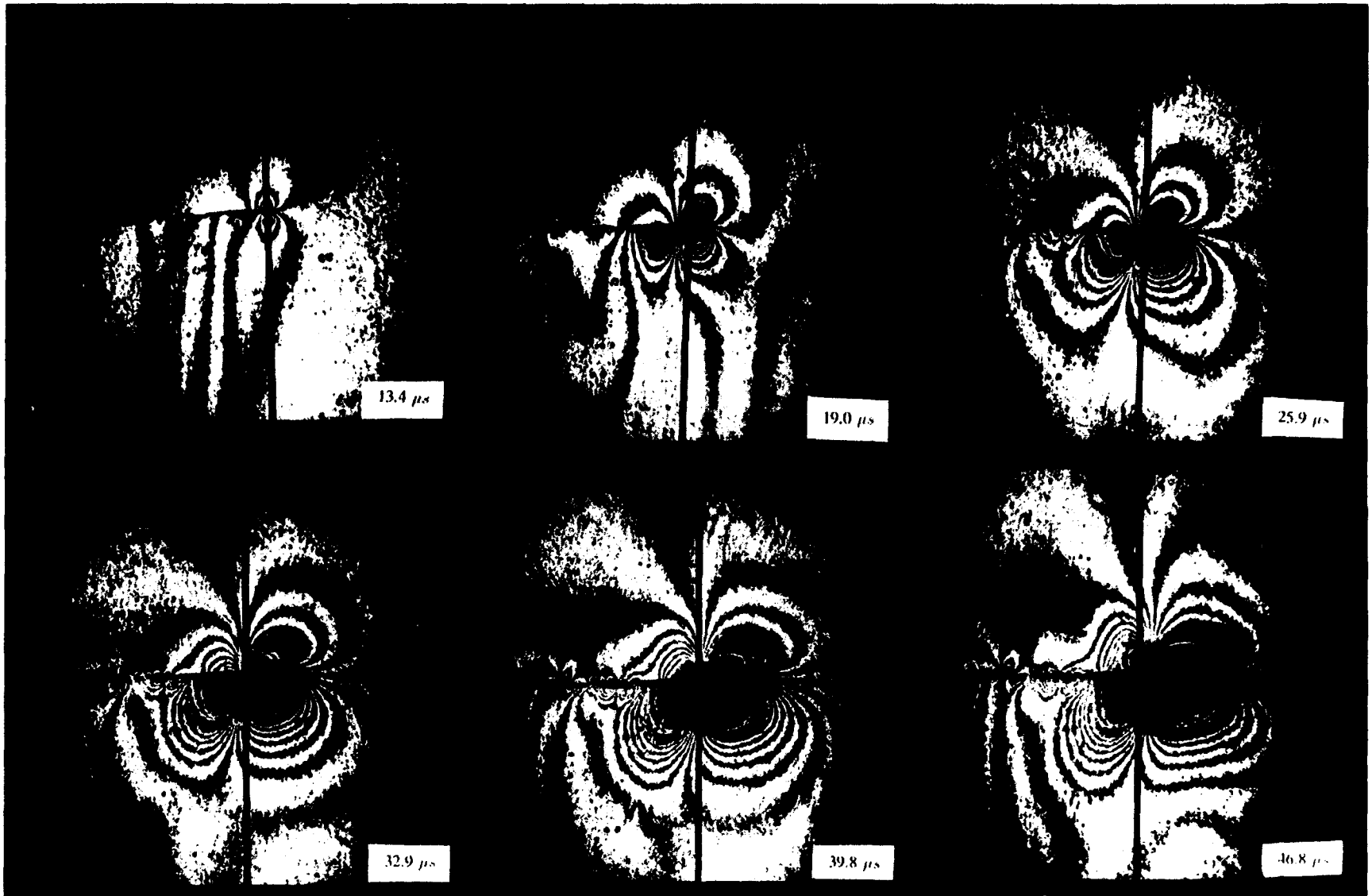

FIGURE 8 Sequence of CGS interferograms corresponding to the initial stages of the dynamic asymmetric loading of the pre-cracked specimen impacted at 38 m/s.

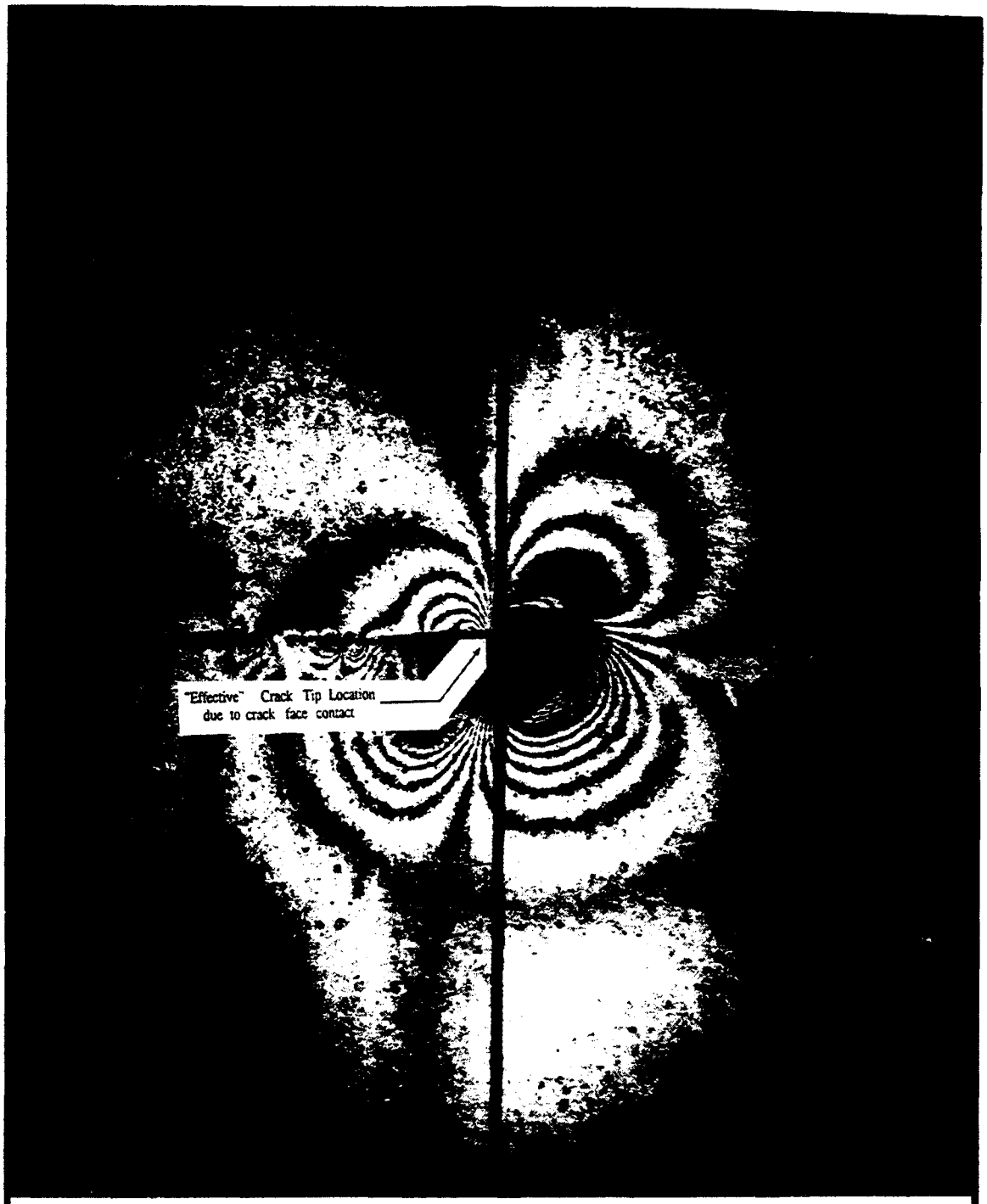

The actual initial crack tip, as indicated, and the "effective" initial crack tip can be seen in this photograph

FIGURE 9

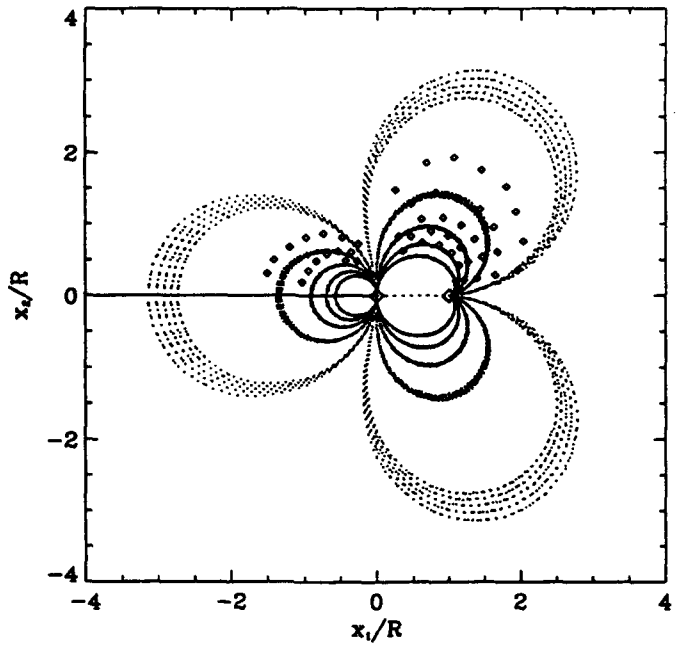

FIGURE 10 A check of the fitting procedure for t=31.5 μsData points should fall alternately on light and dark fringes in the figure. It can be seen that the fit is reasonably good for the forward fringe with less agreement found for the rear fringe.

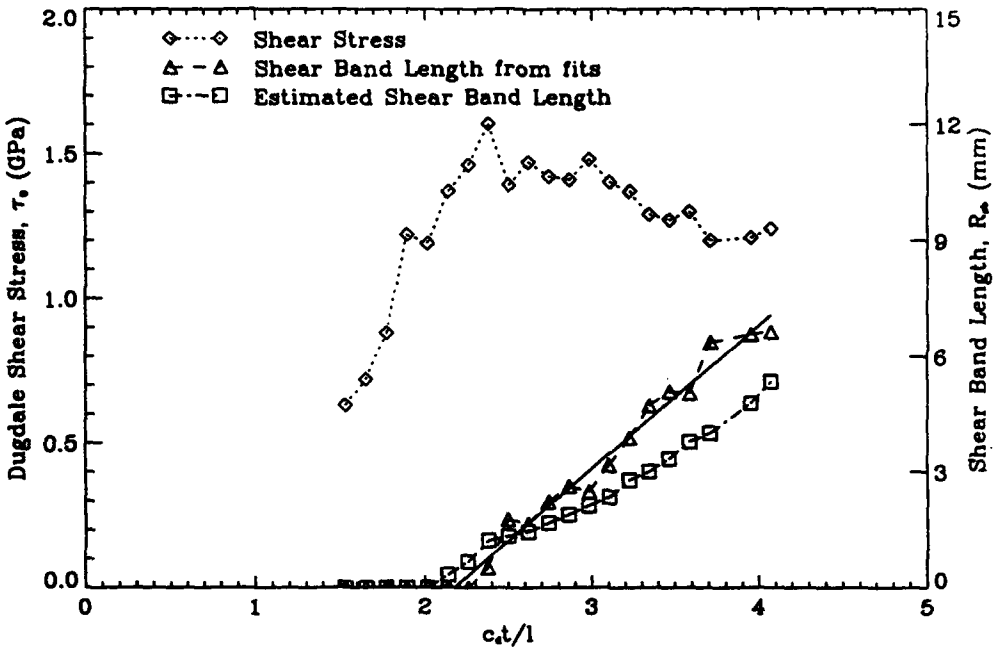

FIGURE 11 A plot of $\tau_0(t)$ and $R(t)$ as found from the fitting procedure in equation (12). The shear band length is compared to the length as estimated by comparing the fringe patterns in Figure 8 to the theoretical fringe pattern in Figure 4.

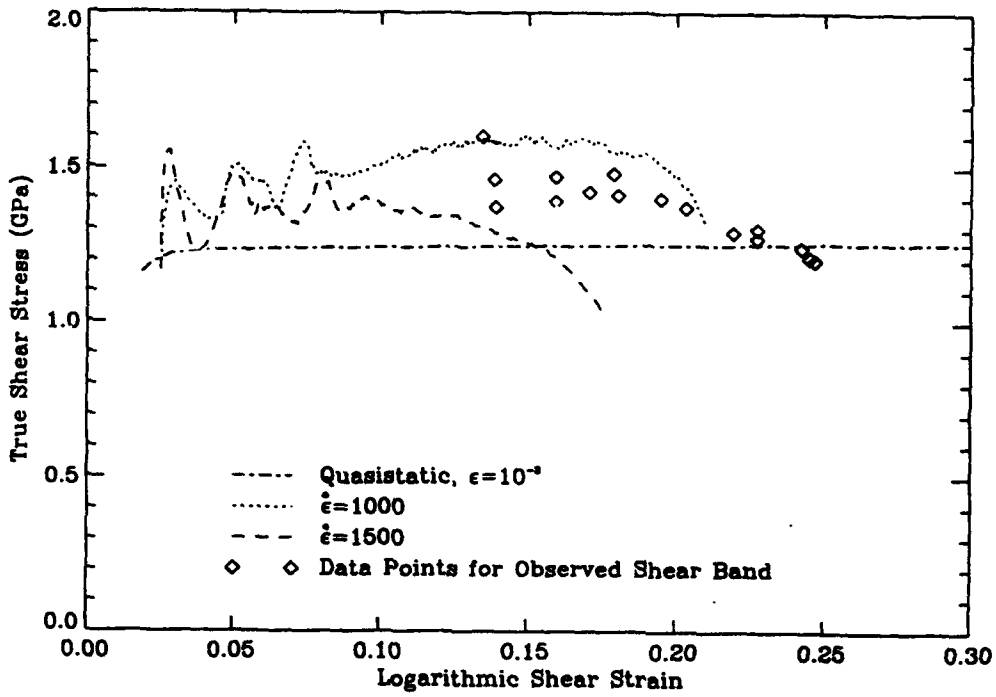

FIGURE 12 The constitutive behavior of C-300 at various strain rates as measured in compression. High strain rate data was measured using a Kolsky bar apparatus as shown in Mason et al. (1992b)